Journal of Wind Engineering & Industrial Aerodynamics 254 (2024) 105906

Contents lists available at ScienceDirect

Journal of Wind Engineering & Industrial Aerodynamics

journal homepage: www.elsevier.com/locate/jweia

Impacts of building modifications on the turbulent flow and heat transfer in urban surface boundary layers

Seika Tanji [a,*], Tetsuya Takemi [a], Guangdong Duan [b]

[a] *Disaster Prevention Research Institute, Kyoto University, Gokasho, Uji, Kyoto, 6110011, Japan*
[b] *Navigation College, Dalian Maritime University, Dalian, 116026, PR China*

ARTICLE INFO

Keywords:
Turbulence
Heat transport
Urban heat island
Large-eddy simulation
Building arrangement

ABSTRACT

This study examines turbulent airflow and upward heat transport in real urban environments using a building-resolving large-eddy simulation model to understand the characteristics of turbulent airflow and upward heat transport when geometrical distributions of buildings are modified. The target areas were two real urban districts within Osaka City, Japan, having different morphological features. In the numerical experiments, the initial condition was set to a neutral condition in which temperature is uniformly distributed vertically, and buildings emitted heat at a constant rate. The results in the two districts indicated that the features of turbulence and heat transport distinctly differed with different building arrangement. Specifically, taller buildings significantly decelerated airflows and induced warming behind buildings. More high-rise buildings (which resulted in a larger building variability) in a district with a larger building density caused a large heat flux and warming at higher levels. The sensitivity experiments in which a density and height variability of buildings were modified showed that a building density at higher levels and a building height variability significantly influenced warming at upper levels. An increased building height variability weakened wind speed and disturbed horizontal heat advection, whereas a large building density caused numerous heat sources.

1. Introduction

The urban heat island (UHI) is a phenomenon with which surface temperatures are higher in cities than in their surrounding rural areas (Oke, 1982). Urban heating results from their lower albedo, less water available for evaporative cooling, higher potential for heat storage, and greater heat emissions from buildings and man-made structures, compared with areas having other land uses (Taha, 1997; Chapman et al., 2018). Previous studies have simulated effects of UHI on meteorological fields using meso-scale numerical models (Silva et al., 2021; Oleson et al., 2008; Chapman et al., 2019; Dudorova and Belan, 2022).

Recent studies clarified that local warming by UHI can trigger local-scale rainfall and intensify convective precipitation in urban areas because of the destabilization by boundary-layer warming in urban areas. Lin et al. (2011) evaluated the effects of UHI on precipitation in Taiwan using the Weather Research and Forecasting (WRF) model coupled with an urban canopy model. They pointed out that reproducing precipitation under the UHI conditions required an accurate land-use classification. Steensen et al. (2022) examined precipitation in city areas under the influences of UHI in historical and future climate scenarios. They demonstrated that UHI-induced precipitation decreased in a warmer future climate compared with a historical climate condition. These studies demonstrated that the UHI had an impact on precipitation patterns in urban areas from a mesoscale point of view. In addition, the effects of the UHI on precipitation should also be investigated from a microscale point of view through examining upward heat transports influenced by building structures, which may contribute to triggering convective clouds and precipitation.

In the atmospheric boundary layer influenced by the UHI, turbulence plays an important role in transporting momentum, heat, water vapor, pollutants etc. to upper levels. Turbulence in the atmospheric boundary layer develops through mechanical and/or thermal generation. The mechanical generation of turbulence is determined mainly by vertical gradients of winds that are due to the friction near the ground. This process is more complicated in densely built urban districts because of variable spatial gradients of winds especially around building walls. Buoyancy generated by atmospheric heating develops the thermal generation of turbulence. In urban districts, buildings and man-made structures as well as the ground surface serve as heat sources for the urban boundary layer, which critically depends on the geometrical

---

[*] Corresponding author.
E-mail addresses: seika@storm.dpri.kyoto-u.ac.jp (S. Tanji), takemi@storm.dpri.kyoto-u.ac.jp (T. Takemi), g.duan@my.cityu.edu.hk (G. Duan).

https://doi.org/10.1016/j.jweia.2024.105906
Received 8 March 2024; Received in revised form 24 September 2024; Accepted 25 September 2024

distribution of buildings and structures (Ichinose et al., 1999; Dong et al., 2017). Formation of stagnant flows within densely build environments also influences heat transfer. Duan and Takemi (2021) examined gustiness in the urban boundary layers under stably and unstably stratified conditions, demonstrating that gustiness increased monotonically with boundary-layer instability in unstable conditions while plateaued in stable boundary layer. Therefore, both turbulence generation processes interact with each other and are influenced by building arrangement in urban areas. In the numerical models, reproducing turbulent transport of momentum and heat in the urban boundary layer caused by these processes requires resolving explicitly arrangement of buildings when simulating.

The building arrangement in urban areas is characterized by various geometrical parameters such as maximum building height H_{max}, average building height H_{ave}, plan area density λ_p, and variation of the building height σ (Nakayama et al., 2011; Duan and Takemi, 2021). Previous studies examined the relationship between these parameters and features of turbulence and heat transport by conducting building-resolving large-eddy simulations (LESs). For example, Yoshida et al. (2018) investigated the relationship between building arrangement parameters and turbulent flow structures in Kyoto, Japan. Kanda et al. (2013) precisely estimated drag over Tokyo. Duan et al. (2023) examined turbulent structures in real urban cities to connect ventilation with urban geometrical features. Park et al. (2015a) compared features of airflow and turbulent momentum fluxes in downstream areas of apartment complexes, behind high-rise buildings, and in a park area in a real city and identified their distinct characteristics depending on geometrical natures of each district within a city. These studies revealed that the influence of urban geometrical features on wind speed and turbulence structures appeared differently in real urban areas (Giersch et al., 2022; Wang et al., 2024). However, these previous studies mentioned above examined flows primarily under neutral conditions and did not consider heat emission and transport.

Other previous studies have investigated turbulent airflow and heat transports in urban boundary layers under various stability conditions (Duan and Ngan, 2019; Hong and Lin, 2015). For example, Park and Baik (2013) explored the structure of turbulent flows in unstably stratified environments, while Duan and Takemi (2021) quantified the relationship between airflow variability and urban geometrical features in a real urban district (Osaka, Japan). Pedestrian-level thermal environments have also been a focus of research. Wang et al. (2021) investigated how urban geometrical features and thermal conditions influenced pedestrian-level ventilation, and Oh et al. (2024) examined the combined effects of the UHI on thermal comfort in Seoul, Korea. Mortezazadeh et al. (2021) assessed an impact of urban heatwaves on thermal conditions around buildings in real urban settings. Although these studies have advanced our understanding of turbulent airflow and heat transfer in urban environments, they have primarily focused on ground-level heat exchanges. The role of upward heat transport, particularly in connection to urban heat emissions from buildings, has not been extensively addressed. This upward heat transport plays a critical role in urban meteorology by potentially triggering localized rainfall events. Addressing this gap is essential to advancing our understanding of the UHI effects and its broader meteorological impacts.

The purpose of this study was to investigate the impacts of the urban geometrical features on turbulence and upward heat transport in real urban districts. Urban heating was represented with the heat release from building surfaces; we ignored the sensible heat flux from the ground surface to reveal the influence of building-façade heating. Real urban geographical information data were used as the building geometry. A building-resolving LES model was used to simulate airflow and upward heat transfer in two actual urban districts, with the real building geometry explicitly resolved. We conducted sensitivity experiments with the urban geometry varied through changing the density and height of buildings.

This paper is organized as follows. Section 2 describes the actual urban areas and the configuration of the LES model. Section 3 presents the results of the numerical simulations. Conclusions are given in Section 4.

2. Numerical model and simulation setups

2.1. Numerical model and experimental configurations

We used PALM (Parallelized Large-eddy Simulation Model) v22.10 (Maronga et al., 2020) which was developed by Leibniz Universität Hannover, Germany. PALM solves the Navier-Stokes equations with the Boussinesq approximation in a non-hydrostatic, incompressible framework. A 1.5-order closure scheme of Deardorff (1980) was implemented as the subgrid-scale model of turbulence.

To generate turbulence, we conducted experiments comprising two stages: the precursor and the main run. The precursor run was intended to generate a fully developed turbulent inflow for the main run by employing the periodic lateral boundary conditions for the precursor computational domain. The boundary condition at the inlet of the main run was the Dirichlet condition combined with the turbulence recycling method (Lund et al., 1998; Kataoka and Mizuno, 2002). This recycling method extracted turbulent components $\varphi'(y,z,t)$ from a recycling plane at a fixed location x_{rec}, which was a distance from the inlet. $\varphi'(y,z,t)$ was computed by

$$\varphi'(y,z,t) = \varphi(x_{rec},y,z,t) - \langle\varphi\rangle_y(z,t), \tag{1}$$

where $\langle\varphi\rangle_y(z,t)$ was the averaged prognostic variables along the y (spanwise) direction at $x = x_{rec}$. The inflow profiles $\varphi_{inlet}(y,z,t)$ were computed using $\varphi'(y,z,t)$ and $\langle\varphi_{inlet}\rangle_y(z)$ as

$$\varphi_{inlet}(y,z,t) = \langle\varphi_{inlet}\rangle_y(z) + \varphi'(y,z,t). \tag{2}$$

At the outflow boundary, the velocity components satisfied the radiation boundary conditions.

We configured a three-dimensional computational domain on the Cartesian coordinates with the eastward direction (streamwise) defined as the x-axis, the northward direction (spanwise) as the y-axis, and the vertical direction as the z-axis. No-slip boundary conditions were applied for the velocity components on solid surfaces, and Neumann boundary conditions were imposed at the domain top. Neumann boundary conditions were also applied for the potential temperature at solid boundaries. Periodic boundary conditions were imposed at the lateral boundaries along the y-axis. The bottom boundaries and the walls of all buildings were Neumann conditions for potential temperature. We implemented the Monin–Obukhov similarity theory near solid surfaces with a roughness length of $z_{0,m} = 0.1$ m for the momentum and scalars (Park et al., 2015b; Duan et al., 2023).

We prescribed a pressure gradient in the x-direction with the amount of $\Delta P = 0.6 \times 10^{-3}$ Pa m^{-2} between the inflow and outlet boundaries, and thus streamwise airflow was east direction. Initially, a uniform potential temperature ($\theta = 300$ K) throughout the computational domain was prescribed. Under these conditions, the wind speed reached approximately 10 m s^{-1} above 100-m height if no-building surface.

Two areas were chosen within Osaka City for the present LESs (described later in Section 2.3). We conducted two numerical experiments for each area: one with heat emission (referred to as HE) and one without heat emission (referred to as NH). In the NH experiment, no heat flux was prescribed throughout the computational domain. In the HE experiments, constant heat flux at a rate of 0.02 K m s^{-1} was set to emit at all buildings. The magnitude of this heat flux was equivalent to about 23 W m^{-2}, which was comparable with the artificial exhaust heat estimated by Moriwaki and Kanda (2005). The configuration in this study served as a somewhat idealized boundary condition for the heat flux, deliberately excluding sensible heat flux from the ground surfaces. This simplification of excluding flux from the ground surface is to isolate and focus on the impact of heat transport caused solely by building arrangement. Considering sensible heat flux would obscure the effect of the building arrangement near the surface, because the amount of sensible heat flux from the ground surface is about three times larger than that from building surfaces (Moriwaki and Kanda, 2005).

The horizontal grid spacing was $\Delta x = \Delta y = 2$ m. In the vertical direction, the grid spacing was $\Delta z = 2$ m below the 80-m height and was vertically stretched with a factor of 1.08 above the 80-m height, resulting in the maximum Δz of 16 m. The total number of vertical layers was 82, yielding a domain height of about 500 m. An iterative multigrid scheme was used to solve the Poisson equation for the perturbation pressure. We used the 5th-order upwind scheme of Wicker and Skamarock (2002) and the third order Runge-Kutta scheme for the momentum equation. The integration times were 21,600 s (6 h) for the precursor run to spin-up the boundary-layer flow and another 3600 s (1 h) for the main run. We analyzed the results obtained from 3600 s integration in the main run. The sampling duration, i.e. 3600 s beyond a 6 h precursor run, had proven sufficient for ensuring a fully developed turbulent boundary-layer flow over idealized and real urban topographies (Wang et al., 2023; Duan et al., 2023). The sampling interval was set to be 10 s, which has proven suitable for satisfactory separation of adjacent correlated motions for canyon flow developed over roughness elements mounted on the ground surface.

Horizontal computational domains covered an area of $x\times\ y = 1184\ \mathrm{m} \times 544\ \mathrm{m}$ in the main runs. The domain in the main run was wider along the streamwise direction than in the precursor run to prevent numerical instability near the outlet of the radiation boundary condition. The focused urban domains were set in a $500\ \mathrm{m}\times\ 500\ \mathrm{m}$ area, surrounded by a buffer zone of 86 m around the inflow boundary of the x-direction and 22 m both side of the boundaries of the y-direction (Duan et al., 2023). Regularly distributed roughness blocks, each 10 m in height, were placed in the buffer zone to maintain inflow turbulence structures. Around the outlet boundary had a longer buffer zone to ensure computational stability.

2.2. Urban computational domains and building data

The building distributions in the real urban districts in Osaka City, Japan were based on the Geographic Information System data consisting of Digital Elevation Model (DEM) and Digital Surface Model (DSM) data at 2-m resolution, obtained from Kokusai Kogyo Co., Ltd. In the present numerical simulations, we selected two business districts within Osaka as areas having distinct geometrical features with each other: an area around Osaka Station (OS) in the northern part of Osaka City, and an area around Kyocera Dome Osaka (KD) in the western part of Osaka City (Fig. 1a and b, respectively). Fig. 2 illustrates the frequency of building height, as well was the values of some urban morphological parameters in each calculation domain. The parameters chosen here are the maximum building height (H_{max}), the averaged building height (H_{ave}),

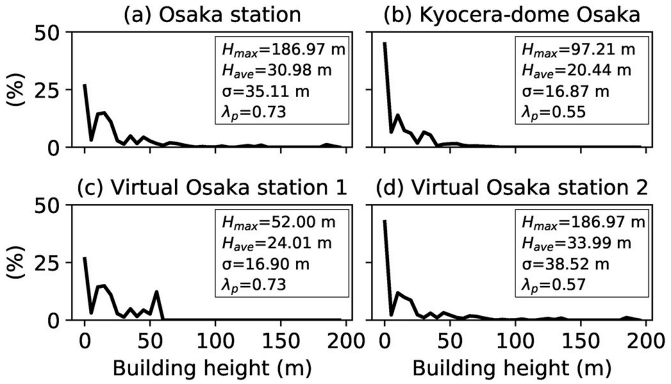

Fig. 2. The frequency distribution of the building height in the (a) OS, (b) KD, (c) V-OS1, and (d) V-OS2 areas, with the values of some urban morphological parameters listed in the inset of each panel. The indicated parameters in the insets are: the maximum building height (H_{max}), the averaged building height (H_{ave}), the building height variability (σ), and the plan area index (λ_p).

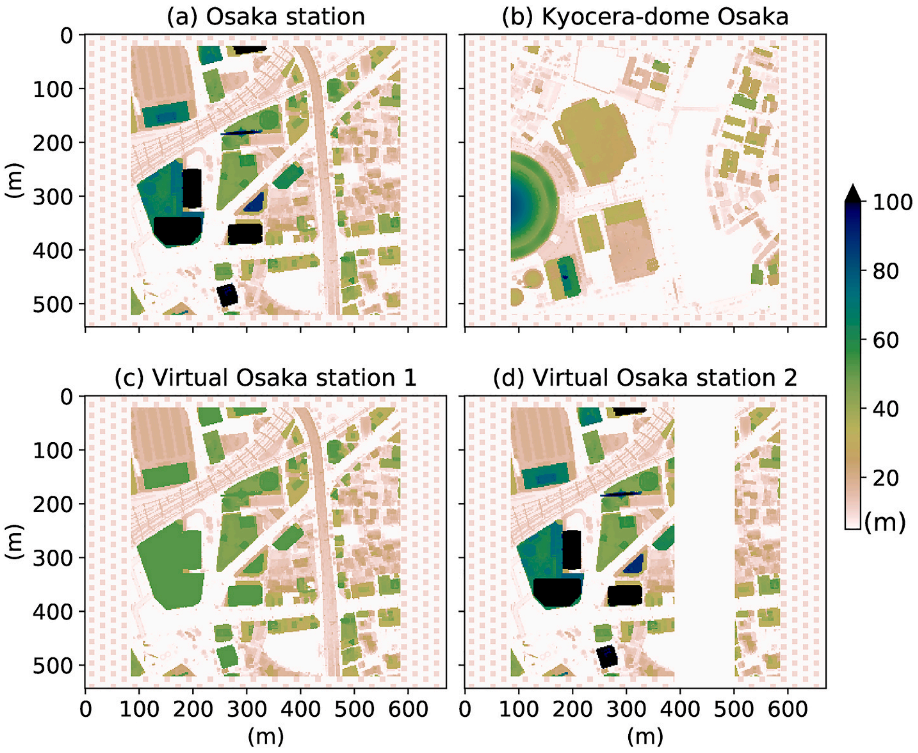

Fig. 1. Building height of the calculation domains around (a) Osaka Station (OS), (b) Kyocera-dome Osaka (KD), (c) Virtual Osaka Station 1 (V-OS1), and (d) Virtual Osaka Station 2 (V-OS2). Upward is the north direction.

the building height variability (σ), and the plan area index (λ_p). Building height variability was defined as the standard deviation of building heights within the calculation domain. Noted that the sum of the values along the x-axis of Fig. 2 was equal to the value of λ_p. The OS area contained 5 high-rise buildings whose tops exceeded the height of 100 m, with the average building height buildings H_{ave} being about 30 m and the building height variability being about 35.11 m. These parameters were larger than that in KD (Fig. 1a, 2a and 2b). The building packing density, i.e., plan area index λ_p, indicated that 73% of the OS area was covered by buildings. In contrast, the KD area had lower but wider buildings compared with those in the OS area. The building height variability, the plan area index and the average building height in the KD area were smaller than those in the OS area (Fig. 2b).

In addition to these real urban areas, we created virtual areas by modifying the height and packing density of the buildings in the OS area. Buildings taller than 52 m in the OS area were changed into a uniform height of 52 m. This height was chosen to make the height variability of the OS area equivalent to that of the KD area (Fig. 2c); this area is referred to as V-OS1 (Fig. 1c). In another experiment, we adjusted the building packing density to match that of the KD area by removing buildings in certain parts of the OS area (Fig. 2d); this modified area is referred to as V-OS2 (Fig. 1d). The geometrical features of the area with buildings removed appeared to be similar to that of the area between $x = 400 - 500$ m in the KD area, as displayed in Fig. 1d. It was noted that some buildings had discontinuous surfaces, which may seem to impact numerical stability. The choice of the areas was intended to keep the similarity of the urban morphological parameters. We found that the discontinuous buildings did not affect numerical stability; the buffer zone surrounding the urban domains enabled the calculation domains to keep calculating under numerical stability which smoothly generated turbulence at the inflow boundaries.

2.3. Model validation

Previous studies have validated the performance of the PALM model (Abd Razak et al., 2013; Kanda et al., 2013; Wang and Ng, 2018; Duan and Ngan, 2020; Wang et al., 2023). Park and Baik (2013) conducted experiments with and without heat flux from the ground surface in an ideal area covered with roughness blocks. Their simulation results demonstrated that the vertical profiles of wind velocity and temperature in both experiments agreed with the results from the wind tunnel experiment (Uehara et al., 2000). Duan and Takemi (2021) validated turbulent airflows over an urban area using PALM under thermally stratified conditions. They indicated that the estimated gustiness statistically satisfied observed results in the urban turbulent boundary layer according to the local maximum wind speed, wind fluctuation and turbulence intensities and fluxes. He et al. (2022) used PALM to simulate airflow over urban areas and to compare the model outputs with wind-tunnel measurements. Their finding indicated that the coefficient of determination between the model results and the measurements exceeded 0.6, supporting the reliability of PALM to reproduce airflows densely built areas. We indicated especially the results of Duan and Ngan (2018) in the Supplement material. This work compared the result of a PALM simulation and a wind tunnel experiment of Brown et al. (2000) around the canyon (Supplement 1) with the statistical method. LES results of vertical wind profiles within a unit-aspect-ratio street canyon showed excellent agreement with the wind-tunnel data of Brown et al. (2000) (Supplement 2). In addition, values of the normalized mean square error (NMSE) were consistently low, reflecting minimal error, while the fractional bias (FB) remained close to zero, indicating that the model neither overestimated nor underestimated the velocities significantly (Supplement 3). The hit rate (q) further underscored the model's robustness, remaining above 66% for all positions, close to the leeward wall ($x/W = -0.4$), at the canyon center ($x/W = 0$) and near the windward wall ($x/W = 0.4$), where x is the streamwise coordinate and W is the canyon width (Supplement 3). Therefore, PALM is trustworthy for calculating airflow and heat transport in real urban areas and is useful for this study.

3. Results

3.1. Real urban areas

In this subsection, we present the results obtained from the real urban data, focusing on the differences between the NH and HE experiments and between the OS and KD areas.

Fig. 3 displays the time-averaged fields of the NH experiment in the OS and KD areas. The period for the averaging was the entire integration time of the main run (i.e. 3600 s). The horizontal and vertical cross-sections of the OS area revealed that the wind speeds behind the buildings were generally weakened (Fig. 3a and b). This weakening was particularly obvious behind buildings taller than 100 m, as evident in the vertical cross-section (Fig. 3b). The regions between buildings, such as $x = 0 - 150$ m along $y = 300$ m and $x = 60 - 400$ m along $y = 100$ m in Fig. 3a, experienced wind speeds exceeding 3 m s^{-1} on the horizontal plane. The momentum flux leeward of the tall building indicated large magnitudes of both positive and negative values in the OS area (Fig. 3c and d). The KD area exhibited stronger winds at the upper levels than the OS area because of the presence of fewer tall buildings, which resulted in less weakening of winds at upper levels (Fig. 3f). The momentum fluxes in most of the KD area showed negative, and their absolute values were larger than those in the OS area. No-building areas (i.e. $x = 260 - 380$ m on the horizontal plane in Fig. 3g and under 120 m height on the vertical plane in Fig. 3h) exhibited large negative momentum flux because the area above those levels had few buildings, and the vertical gradient of the wind speed was intensified. These results indicated that the KD area had obviously different distribution of wind speed and momentum flux compared with the OS area in both the horizontal and vertical planes.

Previous studies that considered sensible heat flux from the ground surface indicated different characteristics of wind and momentum profiles between under neutral and unstable conditions (Park and Baik, 2013; Wang et al., 2021; Bakkali et al., 2015). However, the time-averaged wind speed and momentum flux in both the OS and KD areas in the HE experiments had less different from those in the NH experiments because heating was represented with release only from building surfaces, and the amount of the heat in this study was small compared with the previous studies, and are therefore not shown here. Instead, the time-averaged upward heat flux and potential temperature from the HE experiments in the OS and KD areas are presented in Fig. 4. The distribution of upward heat flux and potential temperature differed notably between in the OS and KD areas. The heat flux was larger in the OS area than in the KD area, particularly in the downstream region of $x \geq 380$ m (Fig. 4a and b). The potential temperature in the OS area was higher behind the buildings (Fig. 4c) and increased at the upper levels (Fig. 4d). In the OS area, an extremely large potential temperature was observed in some points over and around the building roofs, such as at $x = 300$ m $- 380$ m and at $x \approx 440$ m, as shown in the vertical cross-section along $y = 250$ m (Fig. 4d). These warmed areas, referred to as heat pools hereafter, occurred because the wind speed was reduced behind the buildings (Fig. 3b), and the densely packed points served as multiple sources of heat emissions. Some points in the KD area also led to a large heat flux and potential temperature (Fig. 4e–g); however, there were fewer heat pools, and the upper layer was warmed less extensively compared with the OS area. For example, the region warmed more than 300 K extended to the height above 200-m in the OS area, whereas in the KD area such a warmed layer was limited to the height up to about 170 m (Fig. 4d–h).

Fig. 5 shows the vertical profiles of the mean flow properties averaged in time and area. The vertical profiles of the mean streamwise winds were approximately the same between the NH and HE experiments for both areas (Fig. 5a). As noted previously, earlier studies

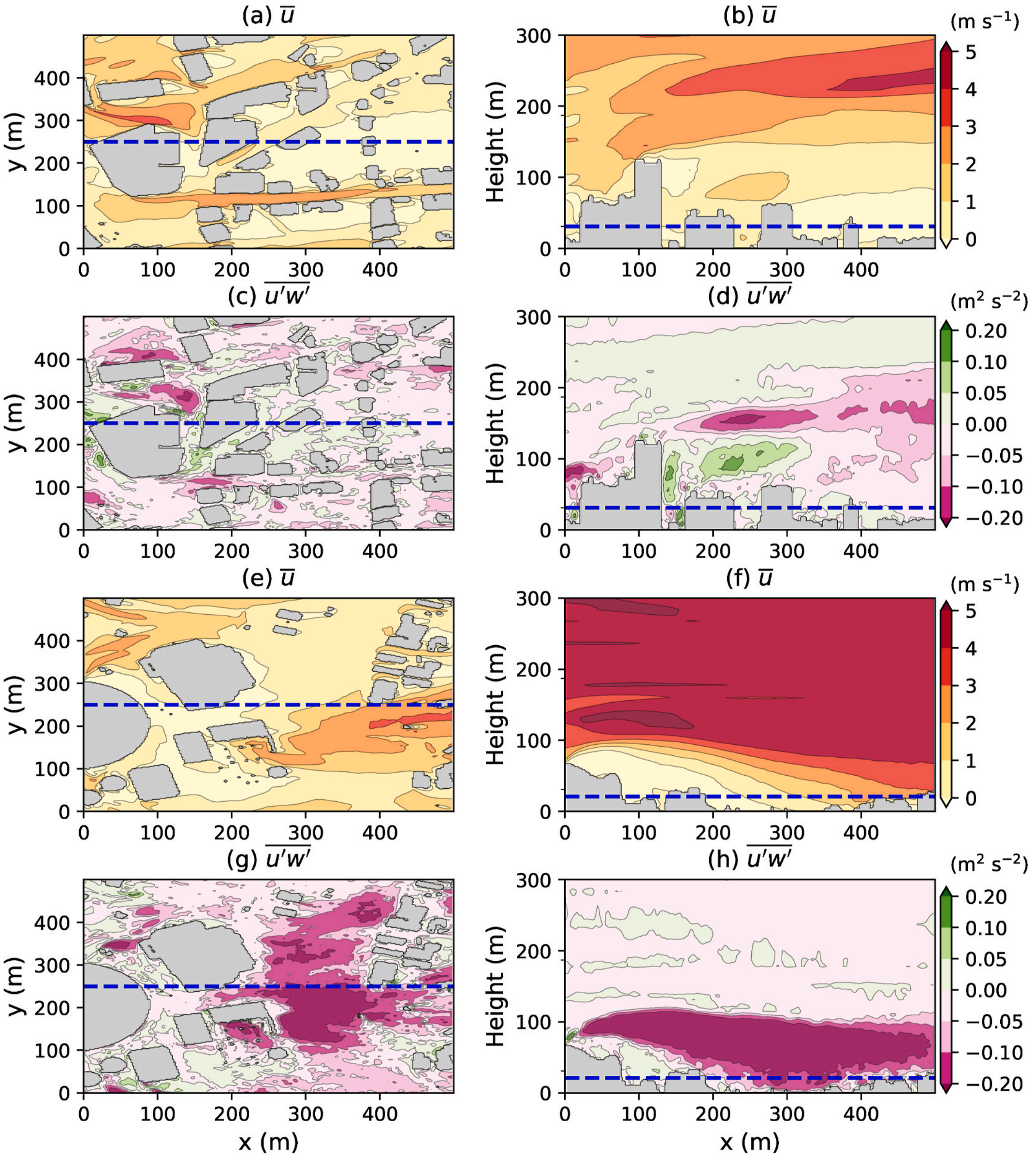

Fig. 3. (a, b, e, f) Time averaged streamwise wind velocity and (c, d, g, h) momentum flux of the NH experiments in the (a–d) OS and (e–h) KD areas. (First column: a, c, e, g) Horizontal cross-section at the average building heights (i.e. $x = 31$ m in the OS area and $x = 21$ m in the KD area). (Second column: b, d, f, h) Vertical cross-section at the center of the calculation domain (i.e., $y = 250$ m).

demonstrated that the streamwise velocity was larger (smaller) around the ground surface (upper levels) in large heating conditions than in no-heating conditions (Park and Baik, 2013; Wang et al., 2021; Bakkali et al., 2015). Park and Baik (2013), which conducted heating experiments around roughness blocks, indicated that the momentum flux was larger with heating than without heating below the height of twice the block height. Our experiments also indicated that the momentum fluxes both the OS and KD areas were larger in the HE experiments than in the NH experiment, but the differences were not substantial (Fig. 5b). These results suggested that the potential temperature was regarded as a passive scalar, probably because of small heat emission prescribed in this study. The vertical profiles of heat flux in Fig. 5c exhibited that the characteristics were similar to the passive scalar profile reported by Akinlabi et al. (2022), which had a clearly peak at about 2 H_{ave} height in each area. The OS area had a larger difference of the momentum flux between the NH and HE experiments than the KD area. The difference of the momentum flux between the simulation with and without heating in the OS area is also mentioned in Section 3.2. Comparing the features in the OS and KD area, the mean winds were stronger in the KD area than in the OS area, especially at heights between 80 and 160 m. Momentum flux exhibited local peaks in both areas (Fig. 5b). A peak in the KD area was observed at 80 m height, corresponding to the maximum building height in the area (see Fig. 2b). In contrast, the OS area showed not a single sharp peak but multiple peaks at ∼ 70 m height and at ∼ 180 m. These levels roughly aligned with the local peaks of the building height in the OS area (see Fig. 2a). The OS area with heating was warmed largely in the upper layer than the KD area, which was confirmed in the vertical profile of the mean upward heat flux and potential temperature (Fig. 5d). Focusing the upward heat flux, the vertically integrated heat fluxes below 400 m height in the OS area was 1.67 times larger than that in the KD areas. The vertical integration was calculated by the trapezoidal rule of the integral for the vertical direction in Fig. 5c. These results suggested that the two districts had different features of the vertical profiles of wind and heat, and the magnitude of the effect of heat emission from buildings on the atmosphere was diverse, despite both being urban areas.

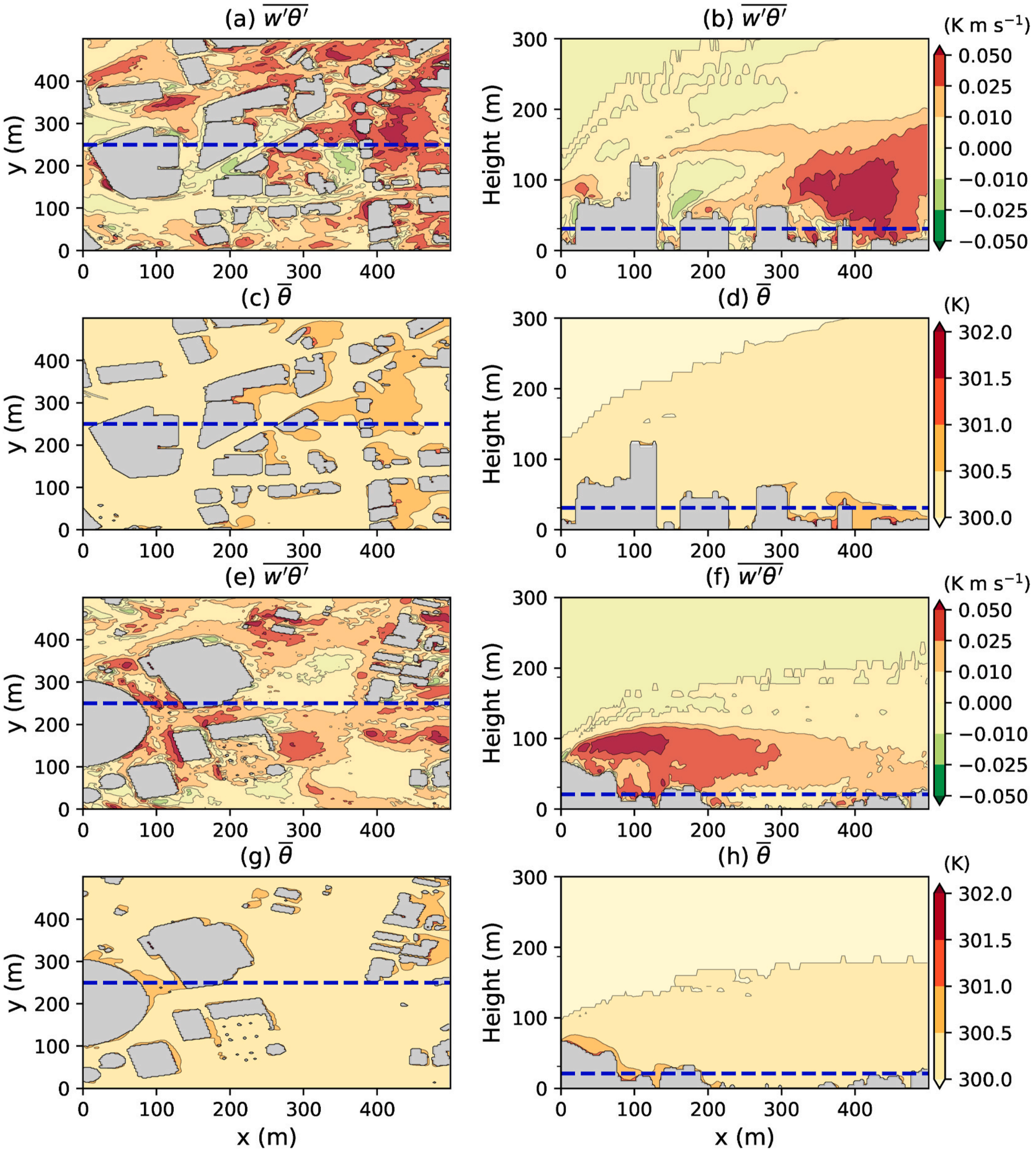

Fig. 4. (a, b, e, f) Time averaged upward heat flux and (c, d, g, h) potential temperature of the NE experiments in the (a–d) OS and (e–h) KD areas. (First column: a, c, e, g) Horizontal cross-section along the average building heights (i.e. $x = 31$ m in the OS area and $x = 21$ m in the KD area). (Second column: b, d, f, h) vertical cross-section along the center of the calculation domain (i.e., $y = 250$ m).

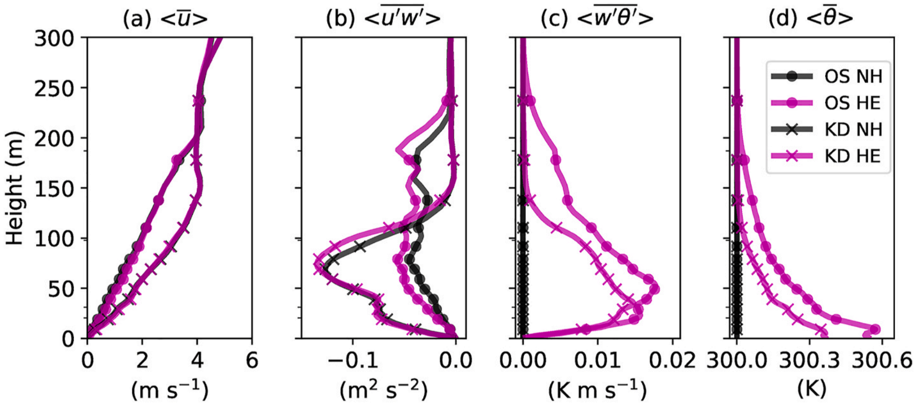

Fig. 5. Vertical profiles of spatial and temporal averaged (a) streamwise velocity, (b) momentum flux, (c) heat flux, and (d) potential temperature. Circle marks and cross marks show the results in the OS and KD areas, respectively. Black and pink lines show the result with the NH and HE experiments, respectively. The marks are plotted every 5-vertical grid.

3.2. Virtual urban areas

In this subsection, we analyzed the properties of the turbulence flow and heat simulated in the virtual urban areas, whereby factors associated with the building arrangement that contributed to the differences in the turbulent flow and heat transport between the OS and KD areas can be more easily identified.

Figs. 6 and 7 show the time-averaged fields of the flow and turbulence properties of the heating experiments conducted in the V-OS1 and V-OS2 areas, respectively. Here, we focused on the HE experiments because the results of the NH experiments were qualitatively similar pattern of wind speed and momentum flux as those of the HE experiments. First, we describe the results obtained in the V-OS1 area where the heights of the high-rise buildings were reduced (Fig. 6). The streamwise velocity in the V-OS1 area was intensified above the maximum building height, resembling the streamwise velocity behavior estimated in the KD area (Fig. 6b and 3f). The absolute value of the momentum flux was also large near the maximum building height in the leeward region, particularly at locations east of $x = 320$ m along the center of the domain (i.e., $y = 250$ m) (Fig. 6d). A large heat flux was estimated at positions from $x = 300$ m to the outlet of the domain on the vertical plane along $y = 250$ m in the V-OS1 area, where buildings were densely packed (Fig. 6e and f). This position corresponded to the large heat flux region in the OS area (Fig. 4a and b). However, the regions of large heat flux and high potential temperature on the vertical plane were confined to lower levels below a height of 200 m (Fig. 6f–h), which was different from the levels with high potential temperature in the OS area (Fig. 4f–h).

Fig. 7 shows the characteristics of the V-OS2 area, which differed from those of the OS area, especially around the region where we removed buildings. The features of the wind velocity were similar to those in the OS area, and the wind speed at the upper level (e.g., 300 m height) exceeded 4 m s^{-1} (Fig. 7b). The regions of larger magnitudes of the momentum flux extended leeward from the tallest buildings and reached the building-removed area (Fig. 7c and d). The heat flux near the surface, from $x = 300$ m – 380 m along $y = 250$ m, was relatively

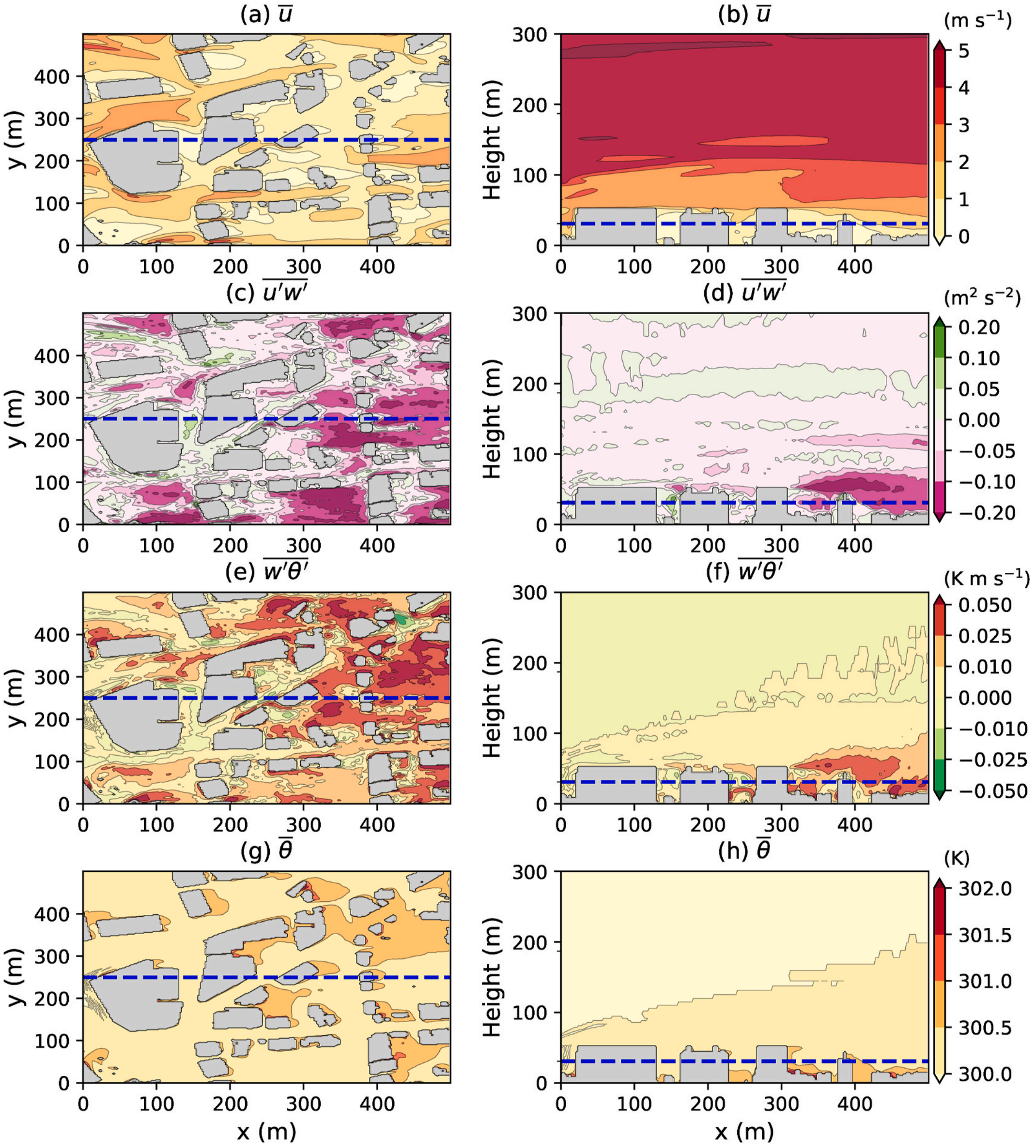

Fig. 6. (a, b) Time averaged streamwise velocity, (c, d) momentum flux, (e, f) upward heat flux and (g, h) potential temperature of the HE experiments in the V-OS1 area. (First column: a, c, e, g) Horizontal cross-section along the average building height of the OS area (i.e. $x = 31$ m). (Second column: b, d, f, h) vertical cross-section along the center of the calculation domain (i.e., $y = 250$ m).

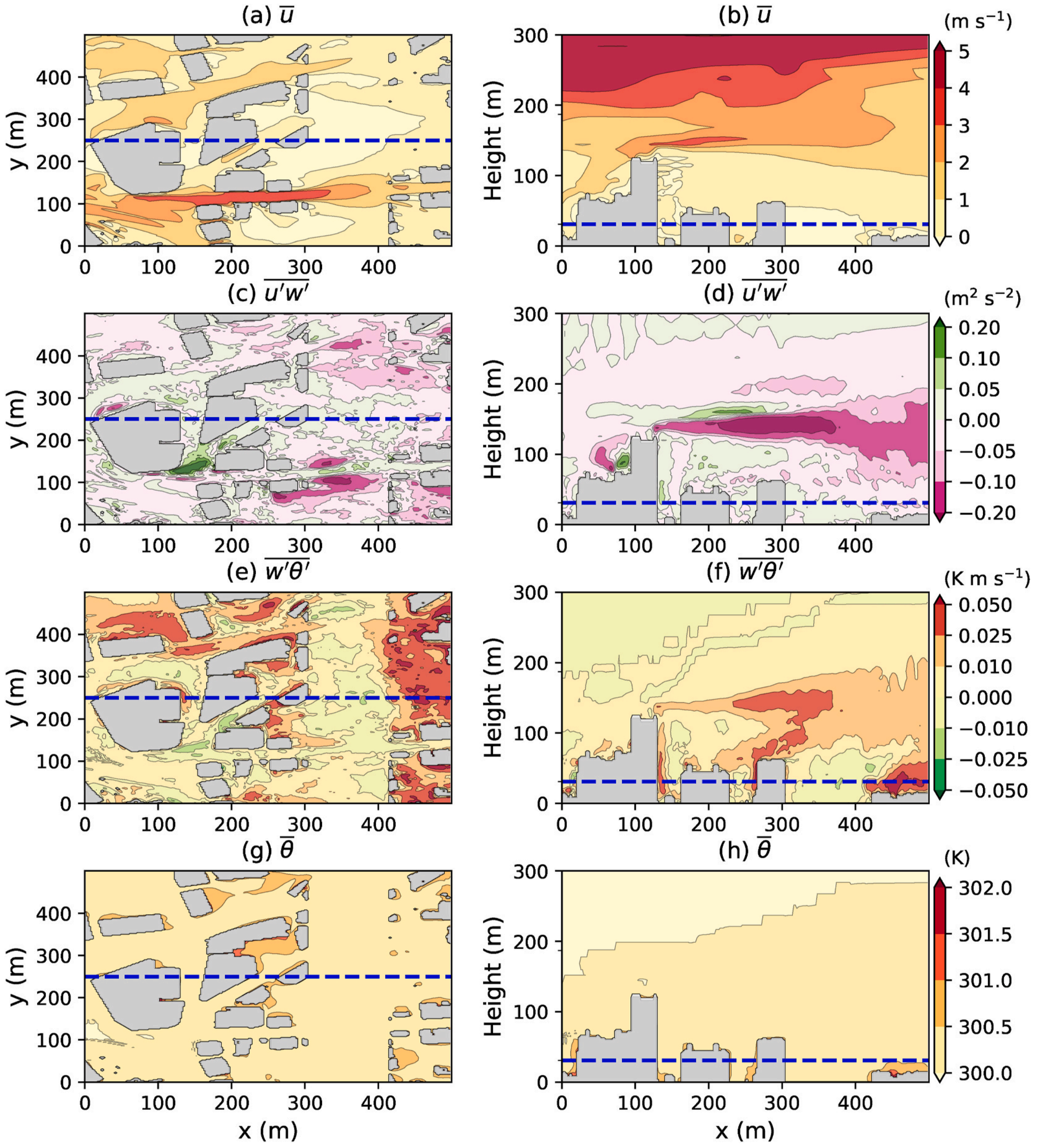

Fig. 7. (a, b) Time averaged streamwise velocity, (c, d) momentum flux, (e, f) upward heat flux and (g, h) potential temperature of the HE experiments in the V-OS2 area. (First column: a, c, e, g) Horizontal cross-section along the average building height of the OS area (i.e. $x = 31$ m). (Second column: b, d, f, h) vertical cross-section along the center of the calculation domain (i.e., $y = 250$ m).

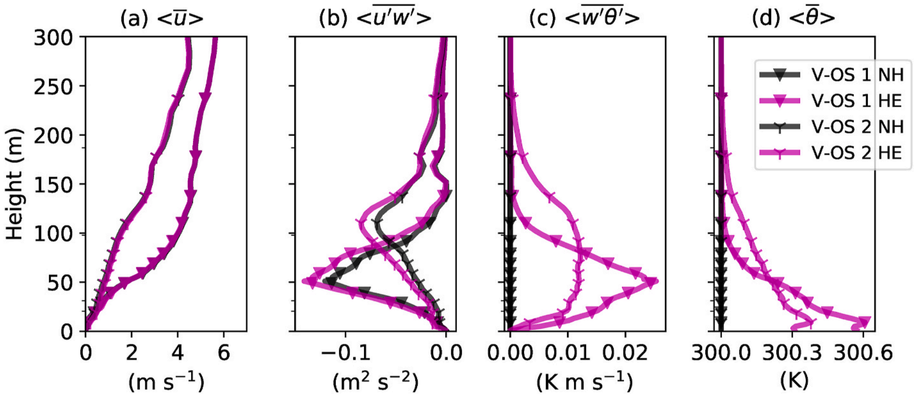

Fig. 8. Vertical profiles of spatial and temporal averaged (a) streamwise velocity, (b) momentum flux, (c) heat flux, and (d) potential temperature. Triangle marks Y character marks represent the result in the V-OS1 and V-OS2 areas, respectively. Black and pink lines show the results obtained with the NH and HE experiments, respectively. The marks are plotted every 5-vertical grid.

small because of the absence of heat-emitting buildings in the area (Fig. 7e and f). However, the upper levels on this plane indicated a larger heat flux over 0.01 K m s^{-1} because of lack of tall building obstructions (Fig. 7f). For the potential temperature, the boundary of 300 K was lower than that in the OS area, but higher than that in the V-OS1 area (Fig. 7h).

These characteristics of streamwise wind speed, momentum flux, heat flux, and potential temperature can be more clearly observed in the vertical profiles of the temporally and horizontally averaged properties (Fig. 8). The profile of the streamwise velocity in the V-OS2 area was approximately the same profile as that in the OS area; however, in the V-OS1 area, it was intensified above the maximum building height of 52 m. This height corresponded to the height having the sharpest peak of the momentum flux in the V-OS1 area. These results demonstrated that lower building height variability clearly caused intensified wind speed and a large absolute value of momentum flux above the maximum building height.

The differences in the wind speed between the simulations with and without heating were very small; however, the differences in the momentum flux were slightly shown, particularly in the areas of large building height variability such as the OS and V-OS2 areas. When the difference in momentum flux is evaluated through integrating it vertically, the absolute value for the difference in the vertically integrated momentum flux below 400 m height between with and without heating was larger in the OS area (2.55 m^3 s^{-2}) than that in the V-OS1 area (1.66 m^3 s^{-2}). The rate of heating to without heating was also larger in the OS area (135%) than that the V-OS1 area (123%). Note that the vertical integration was calculated by the trapezoidal rule of the integral for the vertical direction in Fig. 8b.

The upward heat flux profiles in Fig. 8 also indicated that peak values occurred at various heights. These peak heights were slightly lower than those observed in the momentum fluxes. The peak value of the heat flux was largest in the V-OS1 case among all the HE experiments; however, in this case, the heat flux rapidly decreased above the peak height and became about zero at a height of around 150 m (Fig. 8c). Correspondingly, the potential temperature in the V-OS1 area sharply decreased above the peak height of the heat flux (Fig. 8d). These features in the V-OS1 area were caused by a large advection speed of heat due to a stronger horizontal wind speed (Fig. 8a) and a smaller emission of heat above the 50-m height (Fig. 1c and 2c). The peak height in the V-OS2 area were not clearly identified with the profile and were generally smaller than those in other two OS cases (i.e., OS and V-OS1) (Fig. 8c). Although the peak values are different between the V-OS1 and V-OS2 areas, the vertically integrated heat fluxes below 400 m height, which were calculated by the same method in the prior section, were almost the same between in the V-OS1 and V-OS2 areas. In contrast, compared with the OS area, the vertically integrated heat fluxes in the V-OS1 and V-OS2 areas are respectively 0.77 and 0.79 times as large as that in the OS area. The potential temperature above the 50-m height in the V-OS2 area was approximately the same as that in the OS area, despite that the value below the 50-m height was smaller than that in the OS area (Fig. 8d). This result was caused by the deleted buildings in the V-OS2 area which were less than 50 m tall, and some of the sources of heat emission from buildings were eliminated below this level (Fig. 1d and 2d). Therefore, a comparison of the results in the OS, V-OS1 and V-OS2 areas revealed two primary causes of upper-level warming. First, weak horizontal wind due to large variability of the building height disturbed horizontal heat transport from the buildings and encouraged upward heat transport. Second, the greater building density at higher levels caused larger areas of building walls and roofs that emitted heat. These factors associated with the building distribution led to the OS area warmed at upper levels more largely than the KD area in the previous sections because the OS area met the two features of urban morphological features above.

4. Conclusions and discussion

We investigated turbulent airflow and heat transport by conducting numerical experiments with and without heat emission from building surfaces in two business districts in Osaka City. PALM was used as a building-resolving LES model. The two districts chosen here were the Osaka Station (OS) area and the Kyocera Dome (KD) area. The OS area was characterized with taller buildings, a larger building height variability, and a larger building density than the KD area. In the experiments with heat emission, a constant heat flux of 0.02 K m s^{-1} was prescribed at all the building surfaces. We also conducted numerical experiments in which the height and density of buildings in the OS area were modified to investigate factors that contributed to the different characteristics in the turbulent flow and upward heat transport between the OS and KD areas. The conclusions are summarized as follows.

1) The simulated characteristics of the streamwise wind velocity, momentum flux, upward heat flux, and potential temperature obviously differed between the OS and KD areas, which was due to the difference in building arrangement between the two areas.
2) The case in the OS area indicated weakened wind speed behind the buildings and a large upward heat flux and high potential temperature at the upper levels. The vertically integrated upward heat fluxes below 400 m height in the OS area was 1.67 times larger than that in the KD areas.
3) These results revealed that the magnitude of the effect of heat emission from buildings on the atmosphere depended on the building arrangement there even if in the same business districts.
4) The results in the V-OS1 and V-OS2 areas indicated that the building density at higher levels and the variability of building significantly influence warming at upper levels. A large building height variability weakened wind speed behind the buildings and disturbed the horizontal advection of heat. A large building density resulted in numerous heat sources. These factors caused the OS area warmed at upper levels.
5) The results in this study suggested that modifying the building arrangement in urban areas can effectively control the characteristics of airflow and heat transport originated from heating of buildings.

In the present study, only two districts were selected to examine turbulent flow and heat transport. However, to generalize the relationship between building arrangement and the characteristics of turbulent flow and upward heat transport, several experiments are desirable which simulate turbulent airflow and upward heat transport in other districts that have a wide variety of urban morphological features. For example, through collecting morphological data for various types of urban areas and conducting numerical simulations of airflows and heat transports in those urban areas, developing empirical equations is required to relate urban morphological parameters and total fluxes within entire calculation domains. These empirical equations should be useful in explicitly estimating the effects of building arrangement on meteorological properties at mesoscale. Such estimates will be conducted by employing the results of the building-solving LES model as the inputs for boundary conditions of the meteorological model. We demonstrated in this paper that the different building arrangement in the urban areas caused distinct characteristics of the wind velocity, momentum and heat fluxes, and potential temperature. However, the conventional meteorological models, which is used to estimate the urban effects by urban canopy models (Kusaka et al., 2001; Martilli et al., 2002; Kondo et al., 2005), do not resolve individual buildings and do not distinguish building arrangement on the urban districts. Combining the building-resolving LES model with the meteorological models directly is impractical because of computing costs; however, the empirical equations can replace the conventional methods to consider the effect of building arrangement with lower computing costs. This approach can be utilized to estimate the UHI effects while explicitly considering the building-resolving effect on the meteorological conditions such as local precipitation patterns in urban areas. Furthermore, such approach has a potential to diagnose meteorological conditions in response to future changes in urban building arrangement. Developing empirical equations to quantify the effect of building arrangement on meteorological properties is a challenging and valuable task. We leave it as a topic of future works.

The findings of this study can be novel contribution to the UHI field by demonstrating that artificial modifications of building arrangement in urban areas have a potential to mitigate local heavy rainfall events associated with the UHI. This mitigation is achieved through control of turbulent airflow and heat transport characteristics. If we can control the turbulent flow and heat transport in the boundary layer by modifying the artificial arrangement, the development of instability conditions can be disrupted, thereby reducing the occurrence of local heavy rainfalls in urban districts. Recent research by Yamaguchi et al. (2023) demonstrated that weakening vortex tube by controlling wind velocity could reduce maximum rainfall intensity in a local heavy rainfall event by 27 %. Similar impacts on the boundary layer might be achieved through the modification of building arrangement. Not only modifying the building arrangement but also strategic placement of artificial devices, such as wind turbines (Dörenkämper et al., 2015; Wu and Porté-Agel, 2011) and air boosters, could be effective in changing the features of airflow and heat transport in urban areas.

The experimental design in this paper can be further refined to more comprehensively address the UHI phenomenon. For example, this study considered the heat emission only from building surfaces to evaluate the effects of building arrangement. However, heat flux from the ground surface is generally larger than that from building surfaces (Moriwaki and Kanda, 2005). The changes of albedo resulting from urbanization also influence the UHI. To fully understand the impact of human activities, these factors must be considered and cannot be overlooked.

Funding

This work was supported by JST Moonshot R&D [JPMJMS2283] and Natural Science Foundation of Liaoning Province of China [2022-KF-18-07] (Key Program for Science and Technology Innovation).

Availability of data and materials

The datasets used during the current study are available from the corresponding author on reasonable request.

CRediT authorship contribution statement

Seika Tanji: Writing – original draft, Validation, Methodology, Formal analysis. **Tetsuya Takemi:** Writing – review & editing, Validation, Funding acquisition. **Guangdong Duan:** Writing – review & editing, Validation, Methodology.

Declaration of competing interest

The authors declare that they have no known competing financial interests or personal relationships that could have appeared to influence the work reported in this paper.

Data availability

Data will be made available on request.

Acknowledgments

We thank Dr. Kosei Yamaguchi and Dr. Takemasa Miyoshi for providing insightful comments in the early stage of this study. The simulations were conducted on the supercomputer of ACCMS, Kyoto University.

Abbreviations

DEM	Digital Elevation Model
DSM	Digital Surface Model
FB	fractional bias
LES	large-eddy simulation
NMSE	normalized mean square error
PALM	Parallelized Large-eddy Simulation Model
UHI	urban heat island
WRF	Weather Research and Forecasting

Appendix A. Supplementary data

Supplementary data to this article can be found online at https://doi.org/10.1016/j.jweia.2024.105906.

References

Abd Razak, A., Hagishima, A., Ikegaya, N., Tanimoto, J., 2013. Analysis of airflow over building arrays for assessment of urban wind environment. Build. Environ. 59, 56–65.

Akinlabi, E., Maronga, B., Giometto, M.G., 2022. Dispersive fluxes within and over a real urban canopy: a large-eddy simulation study. Bound-Layer Meteorol 185, 93–128.

Bakkali, M., Inagaki, A., Ashie, Y., Yoshida, Y., Kanda, M., Raasch, S., 2015. Thermal large eddy simulation with sensible heat flux distribution form various 3D building geometries. J Japan Society Civil Eng 71 (4), I_433–I_438.

Brown, M.J., Lawson Jr., R.E., DeCroix, D.S., Lee, R.L., 2000. Mean flow and turbulence measurements around a 2-D array of buildings in a wind tunnel. 11th Joint AMS/AWMA Conference on the Applications of Air Pollution Meteorology. Long Beach, CA.

Chapman, S., Thatcher, M., Salazar, A., Watson, J.E.M., McAlpine, C.A., 2018. The effect of urban density and vegetation cover on the heat island of a subtropical city. J. Appl. Meteorol. Climatol. 57, 2531–2550.

Chapman, S., Thatcher, M., Salazar, A., Watson, J.E.M., McAlpine, C.A., 2019. The impact of climate change and urban growth on urban climate and heat stress in a subtropical city. Int. J. Climatol. 39 (6), 3013–3030.

Deardorff, J.W., 1980. Stratocumulus-capped mixed layers derived from a three-dimensional model. Bound-Layer Meteorol 18, 495–527.

Dong, Y., Varquez, A.C.G., Kanda, M., 2017. Global anthropogenic heat flux database with high spatial resolution. Atmos. Environ. 150, 276–294.

Dörenkämper, M., Witha, B., Steinfeld, G., Heinemann, D., Kühn, M., 2015. The impact of stable atmospheric boundary layers on wind-turbine wakes within offshore wind farms. Wind Eng Ind Aerodyn 144, 146–153.

Duan, G., Nakamae, K., Takemi, T., 2023. Impacts of urban morphometric indices on ventilation. Build. Environ. 229, 109907.

Duan, G., Ngan, K., 2018. Effects of time-dependent inflow perturbations on turbulent flow in a street canyon. Bound-Layer Meteorol 167 (2), 257–284.

Duan, G., Ngan, K., 2019. Sensitivity of turbulent flow around a 3-D building array to urban boundary-layer stability. Wind Eng Ind Aerodyn 193, 103958.

Duan, G., Ngan, K., 2020. Influence of thermal stability on the ventilation of a 3-D building array. Build. Environ. 183, 106969.

Duan, G., Takemi, T., 2021. Gustiness in thermally-stratified urban turbulent boundary-layer flows and the influence of surface roughness. Wind Eng Ind Aerodyn 208, 104442.

Dudorova, N.V., Belan, B.D., 2022. The energy model of urban heat island. Atmosphere 13, 457.

Giersch, S., Guernaoui, O.E., Raasch, S., Sauer, M., 2022. Marta Palomar c,4Atmospheric flow simulation strategies to assess turbulent wind conditions for safe drone operations in urban environments. Wind Eng Ind Aerodyn 229, 105136.

He, Y., Yuan, C., Ren, C., Ng, E., 2022. Urban ventilation assessment with improved vertical wind profile in high-density cities – comparisons between LiDAR and conventional methods. Wind Eng Ind Aerodyn 228, 105116.

Hong, B., Lin, B., 2015. Numerical studies of the outdoor wind environment and thermal comfort at pedestrian level in housing blocks with different building layout patterns and trees arrangement. Renew. Energy 73, 18–27.

Ichinose, T., Shimodozono, K., Hanaki, K., 1999. Impact of anthropogenic heat on urban climate in Tokyo. Atmos. Environ. 33 (24–25), 3897–3909.

Kanda, M., Inagaki, A., Miyamoto, T., Gryschka, M., Raasch, S., 2013. New aerodynamic parametrization for real urban surfaces. Bound-Layer Meteorol 148, 357–377.

Kataoka, H., Mizuno, M., 2002. Numerical flow computation around aerolastic 3d square cylinder using inflow turbulence. Wind Struct. 5, 379–392.

Kondo, H., Genchi, Y., Kikegawa, Y., Ohashi, Y., Yoshikado, H., Komiyama, H., 2005. Development of a multi-layer urban canopy model for the analysis of energy consumption in a big city: structure of the urban canopy model and its basic performance. Bound-Layer Meteorol 116, 395–421.

Kusaka, H., Kondo, H., Kikegawa, Y., Kimura, F., 2001. A simple single-layer urban canopy model for atmospheric models: comparison with multilayer and slab models. Bound-Layer Meteorol 101, 329–358.

Lin, C.Y., Chen, W.C., Chang, P.L., Sheng, Y.F., 2011. Impact of the urban heat island effect on precipitation over a complex geographic environment in northern taiwan. J. Appl. Meteorol. Climatol. 50 (2), 339–353.

Lund, T.S., Wu, X., Squires, K.D., 1998. Generation of turbulent inflow data for spatially-developing boundary layer simulations. J. Comput. Phys. 140, 233–258.

Martilli, A., Clappier, A., Rotach, M.W., 2002. An urban surface exchange parameterization for mesoscale models. Bound-Layer Meteorol 104, 261–304.

Maronga, B., Banzhaf, S., Burmeister, C., Esch, T., Forkel, R., Fröhlich, D., Fuka, V., Gehrke, K.F., Geletič, J., Giersch, S., Gronemeier, T., Groß, G., Heldens, W., Hellsten, A., Hoffmann, F., Inagaki, A., Kadasch, E., Kanani-Sühring, F., Ketelsen, K., Khan, B.A., Knigge, C., Knoop, H., Krč, P., Kurppa, M., Maamari, H., Matzarakis, A., Mauder, M., Pallasch, M., Pavlik, D., Pfafferott, J., Resler, J., Rissmann, S., Russo, E., Salim, M., Schrempf, M., Schwenkel, J., Seckmeyer, G., Schubert, S., Sühring, M., von Tils, R., Vollmer, L., Ward, S., Witha, B., Wurps, H., Zeidler, J., Raasch, S., 2020. Overview of the PALM model system 6.0. Geosci. Model Dev. (GMD) 13, 1335–1372.

Moriwaki, R., Kanda, M., 2005. Annual totals of energy and CO_2 fluxed in a residential area. Annu J Hydraul Eng, JSCE 49, 361–366.

Mortezazadeh, M., Jandaghian, Z., Wang, L.L., 2021. Integrating CityFFD and WRF for modeling urban microclimate under heatwaves. Sustain. Cities Soc. 66, 102670.

Nakayama, H., Takemi, T., Nagai, H., 2011. LES analysis of the aerodynamic surface properties for turbulent flows over building arrays with various geometries. J. Appl. Meteorol. Climatol. 50, 1692–1712.

Oh, G., Yang, M., Choi, J.I., 2024. Large-eddy simulation-based wind and thermal comfort assessment in urban environments. Wind Eng Ind Aerodyn 246, 105682.

Oke, T.R., 1982. The energetic basis of the urban heat island. Q. J. R. Meteorol. Soc. 108 (455), 1–24.

Oleson, K.W., Bonan, G.B., Feddema, J., Vertenstein, M., 2008. An urban parameterization for a global climate model. Part II: sensitivity to input parameters and the simulated urban heat island in offline simulations. J. Appl. Meteorol. Climatol. 47 (4), 1061–1076.

Park, S.B., Baik, J.J., 2013. A large-eddy simulation study of thermal effects on turbulence coherent structures in and above a building array. J. Appl. Meteorol. Climatol. 52 (6), 1348–1365.

Park, S.B., Baik, J.J., Han, B.S., 2015a. Large-eddy simulation of turbulent flow in a densely built-up urban area. Environ. Fluid Mech. 15 (2), 235–250.

Park, S.B., Baik, J.J., Lee, S.H., 2015b. Impacts of mesoscale wind on turbulent flow and ventilation in a densely built-up urban area. J. Appl. Meteorol. Climatol. 54 (4), 811–824.

Silva, R., Carvalho, A.C., Carvalho, D., Rocha, A., 2021. Study of urban heat islands using different urban canopy models and identification methods. Atmosphere 21 (4), 521.

Steensen, B.M., Marelle, L., Hodnebrog, Ø., 2022. Future urban heat island influence on precipitation. Clim. Dynam. 58, 3393–3403.

Taha, H., 1997. Urban climates and heat islands: albedo, evapotranspiration, and anthropogenic heat. Energy Build. 25 (2), 99–103.

Uehara, K., Murakami, S., Oikawa, S., Wakamatsu, S., 2000. Wind tunnel experiments on how thermal stratification affects flow in and above urban street canyons. Atmos. Environ. 34, 1553–1562.

Wang, H., Furtak-Cole, E., Ngan, K., 2023. Estimating mean wind profiles inside realistic urban canopies. Atmosphere 14, 1.

Wang, W., Ng, E., 2018. Large-eddy simulations of air ventilation in parametric scenarios: comparative studies of urban form and wind direction. Architect. Sci. Rev. 1–11.

Wang, W., Sekikawa, T., Okaze, T., Ikegaya, N., 2024. Comparison of various statistical methods for estimating extreme wind speed at the pedestrian level in idealized and actual urban areas. Wind Eng Ind Aerodyn 250, 105778.

Wang, W., Wang, X., Ng, E., 2021. The coupled effect of mechanical and thermal conditions on pedestrian-level ventilation in high-rise urban scenarios. Build. Environ. 191, 107586.

Wicker, L.J., Skamarock, W.C., 2002. Time-splitting methods for elastic models using forward time schemes. Mon. Weather Rev. 130, 2088–2097.

Wu, Y.T., Porté-Agel, F., 2011. Large-eddy simulation of wind-turbine wakes: evaluation of turbine parametrisations. Bound-Layer Meteorol 138, 345–366.

Yamaguchi, K., Nishimura, T., Nakakita, E., 2023. LES of the guerrilla heavy rainfall at toga river, kobe, 2008 and meteorological control by intervention in wind speed field. DPRI Annu 66B (in Japanese).

Yoshida, T., Takemi, T., Horiguchi, M., 2018. Large-eddy-simulation study of the effects of building-height variability on turbulent flows over an actual urban area. Bound-Layer Meteorol 168, 127–153.